University Library

MINERVA ACCESS

A gateway to Melbourne's research publications

Minerva Access is the Institutional Repository of The University of Melbourne

Author/s:
Jakob, AM;Robson, SG;Schmitt, V;Mourik, V;Posselt, M;Spemann, D;Johnson, BC;Firgau, HR;Mayes, E;McCallum, JC;Morello, A;Jamieson, DN

Title:
Deterministic Shallow Dopant Implantation in Silicon with Detection Confidence Upper-Bound to 99.85% by Ion–Solid Interactions

Date:
2022-01-01

Citation:
Jakob, A. M., Robson, S. G., Schmitt, V., Mourik, V., Posselt, M., Spemann, D., Johnson, B. C., Firgau, H. R., Mayes, E., McCallum, J. C., Morello, A. & Jamieson, D. N. (2022). Deterministic Shallow Dopant Implantation in Silicon with Detection Confidence Upper-Bound to 99.85% by Ion–Solid Interactions. Advanced Materials, 34 (3), https://doi.org/10.1002/adma.202103235.

Persistent Link:
https://hdl.handle.net/11343/301751

License:
CC BY-NC-ND

ADVANCED MATERIALS
www.advmat.de

Check for updates

Deterministic Shallow Dopant Implantation in Silicon with Detection Confidence Upper-Bound to 99.85% by Ion–Solid Interactions

*Alexander M. Jakob, Simon G. Robson, Vivien Schmitt, Vincent Mourik, Matthias Posselt, Daniel Spemann, Brett C. Johnson, Hannes R. Firgau, Edwin Mayes, Jeffrey C. McCallum, Andrea Morello, and David N. Jamieson**

Silicon chips containing arrays of single dopant atoms can be the material of choice for classical and quantum devices that exploit single donor spins. For example, group-V donors implanted in isotopically purified ^{28}Si crystals are attractive for large-scale quantum computers. Useful attributes include long nuclear and electron spin lifetimes of ^{31}P, hyperfine clock transitions in ^{209}Bi or electrically controllable ^{123}Sb nuclear spins. Promising architectures require the ability to fabricate arrays of individual near-surface dopant atoms with high yield. Here, an on-chip detector electrode system with 70 eV root-mean-square noise (≈20 electrons) is employed to demonstrate near-room-temperature implantation of single 14 keV $^{31}P^{+}$ ions. The physics model for the ion–solid interaction shows an unprecedented upper-bound single-ion-detection confidence of 99.85 ± 0.02% for near-surface implants. As a result, the practical controlled silicon doping yield is limited by materials engineering factors including surface gate oxides in which detected ions may stop. For a device with 6 nm gate oxide and 14 keV $^{31}P^{+}$ implants, a yield limit of 98.1% is demonstrated. Thinner gate oxides allow this limit to converge to the upper-bound. Deterministic single-ion implantation can therefore be a viable materials engineering strategy for scalable dopant architectures in silicon devices.

1. Introduction

The development of complementary metal–oxide–semiconductor (CMOS) devices in the sub-20 nm regime leads to new applications arising from the control of single charges and spins on individual dopants in silicon. Promising applications are where the donors function as quantum bits (qubits). However, configuring materials with arrays of single donor qubits in the solid state is a formidable challenge. It has been proposed that noisy, intermediate-scale quantum (NISQ)[1] devices with ≈50–100 qubits can surpass classical supercomputers in executing some specific algorithms.[2] Even for NISQ devices, the error budgets for the physical qubits are strict, requiring errors well below 1% in order to achieve sufficient circuit depths. Beyond NISQ, error-corrected, universal quantum processors of the kind necessary to run Shor's factoring algorithm on a 2000 bit classical key will require upwards of 4000 logical qubits. Using a 2D surface code architecture, this would translate to about 200 million physical qubits with present error rates of around 0.1%.[3] Future devices with lower error rates[4] will reduce the required number of physical qubits. The surface code is also able to tolerate 5–10% physically non-functional (absent or faulty) qubits in the architecture.[5,6]

A. M. Jakob, S. G. Robson, D. Spemann, B. C. Johnson, J. C. McCallum, D. N. Jamieson
School of Physics
ARC Centre for Quantum Computation and Communication Technology
University of Melbourne
Parkville, VIC 3010, Australia
E-mail: d.jamieson@unimelb.edu.au

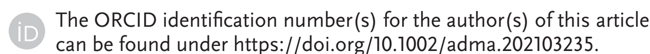
The ORCID identification number(s) for the author(s) of this article can be found under https://doi.org/10.1002/adma.202103235.

© 2021 The Authors. Advanced Materials published by Wiley-VCH GmbH. This is an open access article under the terms of the Creative Commons Attribution-NonCommercial-NoDerivs License, which permits use and distribution in any medium, provided the original work is properly cited, the use is non-commercial and no modifications or adaptations are made.

DOI: 10.1002/adma.202103235

V. Schmitt, V. Mourik, H. R. Firgau, A. Morello
School of Electrical Engineering and Telecommunications
ARC Centre for Quantum Computation and Communication Technology
UNSW Sydney
Sydney, NSW 2052, Australia

M. Posselt
Helmholtz-Zentrum Dresden-Rossendorf (HZDR)
Dresden, 01328 Saxony, Germany

D. Spemann
Leibniz Institute of Surface Engineering (IOM)
Leipzig, 04318 Saxony, Germany

E. Mayes
RMIT Microscopy and Microanalysis Facility
RMIT University
Melbourne, VIC 3001, Australia

 © 2021 The Authors. Advanced Materials published by Wiley-VCH GmbH

Taking these constraints into account, a scalable universal quantum computing platform requires: i) manufacturability at the ≈10^9 physical qubit scale; ii) physical gate error rates at or below 0.1%; iii) no more than a few percent of faulty qubits. Leading technologies including superconducting qubits and ion traps satisfy requirements (ii) and (iii). However, requirement (i) appears extremely challenging for those technologies where the physical qubits are spaced on a scale of several microns.

Classical CMOS silicon devices can be manufactured with billions of transistors on a ≈30 nm pitch[7] and extension to quantum devices could address requirement (i). This has motivated the development of donor spin qubits in silicon,[8] starting from the proposal of Kane.[9] The electron[10] and the nuclear[11] spin of a single ^{31}P donor, ion-implanted in a silicon CMOS device, have proven to be outstanding qubits, with coherence times exceeding 0.5 s (electron) or 30 s (nucleus).[12] Single-qubit error rates are in the 0.01–0.03% range,[13,14] thus addressing requirement (ii) at the 1-qubit level. Conditional two-qubit operations between exchange-coupled donors electrons have been recently demonstrated,[15] as well as universal two-qubit logic gates for donor nuclear spins with sub-1% error rates.[16] In this work, we demonstrate that the industry-standard ion implantation method can be extended to the deterministic implantation of individual dopant atoms with such high confidence to address requirement (iii) for the fabrication of donor qubit arrays with a low density of faulty or absent qubits.

All demonstrations of coherent quantum control of single-donor spin qubits in silicon to date have been achieved in devices where a small number of donors, subject to Poisson statistics, were ion-implanted in the device.[17,18] The number of addressable donor qubits has been observed to reflect the implantation fluence.[15] This follows the well-established precedent of using ion implantation to introduce a well-calibrated density of dopants in classical silicon CMOS devices.[19] We make use of the fact that ion-implanted ^{31}P-atoms in silicon at sparse concentrations can be converted to electrically-active substitutional donors with ≈100% yield[20–22] and sub-2 nm diffusion.[23] This is a present advantage of our donor qubit platforms compared to other spin-based systems in the solid state.[24]

A key benefit of ion implantation is that any group-V donor can be introduced into silicon substrates, allowing a diverse range of applications. The focus of the present work is ^{31}P, the simplest system, offering spin-1/2 nuclear and electron spin qubits.[10–12] Other donors of interest include ^{123}Sb, which has a nuclear spin $I = 7/2$ that can encode error protected logical qubits[25] and can be controlled by local electric fields.[26] Lower-spin donors such as ^{75}As ($I = 3/2$) and ^{121}Sb ($I = 5/2$) could be useful for implementing quantum error detection protocols.[27] Also, ^{209}Bi has a large electron–nuclear hyperfine coupling that results in the formation of noise-protected "clock transitions".[28] Employing these donors in an engineered device requires placing them about ≈7–20 nm beneath the gate oxide interface[29] so that they can be reliably tunnel-coupled to a readout device and electrostatically controlled by metallic surface gates. As a consequence, the kinetic ion implantation energy lies in the range of ≈8–35 keV.

Achieving both deterministic ion implantation of individual donors at such low energy and localization of each implant to high spatial precision is the aim of several strategies that are currently under development. These include the non-stochastic cold-ion trap source[30] where arrays of single ions are assembled before implantation and adaptations of ubiquitous stochastic ion source systems. These include the fly-by image charge detector,[31] where the incidence of a single ion is detected prior to implantation, and strategies where the ion is detected upon implantation. An early example of the latter strategy employs the ion-impact-induced burst of secondary electrons escaping from the substrate surface to signal single-ion implants.[22] However, the yield of secondary electrons is typically below 10 e^-/ion[32,33] at implant energies relevant to device architectures of interest here. This limits the single-ion-detection confidence with conventional secondary electron detectors to ≈90%.[34,35]

In this work we adopt a method that employs signals from the electron–hole (e–h) pairs generated by a single-ion implant into a silicon substrate by utilizing on-chip detector electrodes. The on-chip electrodes form a reverse-biased p–i–n diode, as developed in solid-state detector technologies for ionizing radiation. This method, based on the ion-beam-induced charge (IBIC) principle,[36] is well established for high-energy (of order MeV) ions, but demonstrated here with keV ions.[18,37,38] Thanks to a typical ≈1000 e–h pairs produced by the ion impact, this method has the potential to provide high-confidence signals but, until now, a rigorous quantitative assessment of such confidence has not been developed. Furthermore, here we integrate single-ion detectors and charge-sensitive electronics with an atomic force microscope (AFM) nanostencil scanner (Figure 1 and 2) for precision localization of the implant site.[39] As an example, this system could be employed to fabricate a donor spin qubit architecture that utilizes flip-flop qubits.[40] These are typically placed on a 2D array with 200 nm pitch and coupled by electric dipole interactions (Figure 2c). We further demonstrate that the ion impact signal can also be used to assess the trajectory of the ion species in the substrate material, which is subject to random collision events called straggling. Statistically rare events that result in an undesirable ion placement location can be identified from the signal characteristics with reference to an ion–solid interaction physics model. This unique spectroscopy from IBIC signals distinguishes our method from other deterministic implantation approaches. Used in conjunction with suitable algorithms, capable of signal pulse shape discrimination, could increase the yield of functioning donor qubits in ultrascaled dopant arrays by employing active correction protocols such as conditional implant-repetition steps and dynamic array reconfiguration.

However, to exploit this capability requires charge-sensitive signal processing electronics for the ≈1000 e–h pairs typically generated by each ion impact for near surface implantation. Cryogenic operation of the substrate and electronics is commonly required to achieve sufficiently low detector noise thresholds to reliably observe the signal. However, cryogenic systems are not readily compatible with the integration into ancillary apparatus that must operate at room temperature and can impose considerable operation complexity.

Here, we present a reliable, high-fidelity, counted single-ion implantation system operating near room temperature. For our system with 14 keV $^{31}P^+$ ions, we accurately benchmark the noise and corresponding single-ion-detection confidence of 99.85%. Accounting for ions stopping in the oxide shows controlled silicon doping yield of ≈98%, practical for scalable materials engineering. This material system is compatible with subsequent silicon CMOS processing steps required to fabricate large-scale donor qubit devices.

© 2021 The Authors. Advanced Materials published by Wiley-VCH GmbH

2. Single-Ion Implant System

Our single-ion implantation detector system operates in conjunction with an AFM[42] cantilever stencil that is configured with an ion beam aperture (see **Figure 1**). The sample stage of the AFM holds the silicon substrate chip to be implanted and also incorporates the charge-sensitive electronics coupled to the on-chip single-ion-detector electrodes. The AFM cantilever is controlled by integrated self-actuating technology[43] instead of conventional laser-based optical schemes, which are incompatible with the on-chip detectors as they would be swamped by light spillage. Additional benefits include a more compact and sturdy AFM design that is less sensitive to thermomechanical drift. The AFM cantilever employs tapping mode[44] to approach and image the substrate. This approach is benign compared to more invasive techniques such as electron microscopy, which could inject excess charge and degrade the gate oxide passivation.

Configuration of the AFM cantilever with the stencil aperture is done by milling with a focused ion beam (FIB).[45] For the results presented here, we employed a 16 µm diameter aperture because we sought to investigate the physics of the ion–solid interaction from ion impact signals that are randomly distributed across the sensitive detector area while avoiding detector edge effects. However, cantilevers configured with ≈10 nm apertures, to form a nanostencil, are readily available. For future applications arrays of single donors can be constructed by stepping the nanostencil in response to the detector signals. The AFM cantilever is operated by a monolithic top stage with an independently controllable travel range of $18 \times 18 \times 8$ mm in all three dimensions. This top stage allows a rapid and precise alignment of the cantilever aperture with respect to the incident ion micro-beam, which has ≈22 µm diameter. The much larger cantilever dimension of 350×120 µm^2 blocks the remainder of the ion beam and ensures that no unintentional ion strikes occur outside the aperture.

3. Single-Ion Implant Detectors

The device for implantation is mounted on a circuit board that also contains the charge-sensitive preamplifier electronics. This assembly is mounted on the AFM stage within a Faraday shield containing a thermo-electric Peltier cooler for the detector operation at 263 K (–10 °C). An opening in the shield enables access for the AFM cantilever and the stage provides a 60×60 µm^2 lateral travel range with nominally 5 Å repeated positioning accuracy. The entire AFM assembly is mounted on a positioning stack with ±15 mm lateral travel. This allows coarse positioning between sample and cantilever with nominally ≈50 nm placement accuracy. The AFM image of the circular single-ion implantation area is shown in Figure 1d. The topography map demonstrates the required uniformity of the surface needed for ion implantation of the near-surface donors. The atomic force microscopy image can also identify location markers (not shown here) to align the cantilever ion aperture with the required implant sites to high precision.

Our substrate material employs four separate circular construction sites (configuration I in **Figure 2**a) for the controlled

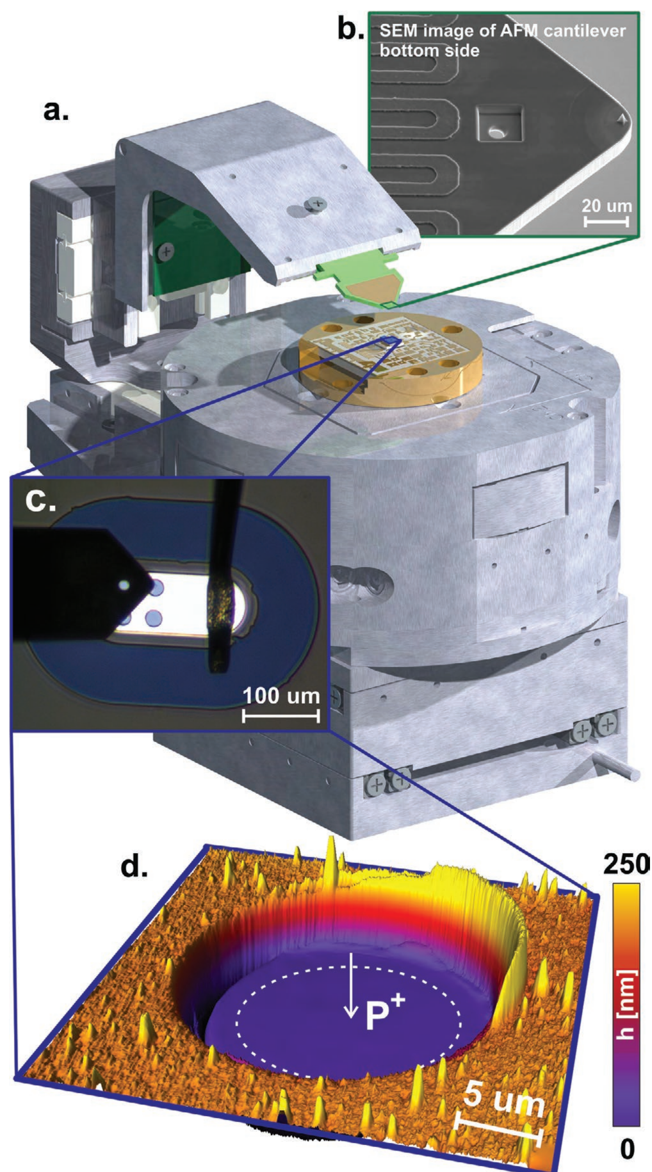

Figure 1. The single-ion implanter system a) The system incorporates an AFM, where the integrated sample stage also houses the charge-sensitive preamplifier electronics.[41] The stage incorporates Peltier cooling to 263 K. b) SEM image of the AFM cantilever (see text). For the present study we configured the cantilever as a stencil by drilling a circular microaperture of 16 µm in diameter, sufficient to localize the ion beam entirely within a single construction site. c) In situ optical AFM camera view, showing the wire bond connecting the single-ion-detector top electrode to the charge-sensitive preamplifier circuit board, housed within the sample stage. The cantilever aperture is concentrically aligned with one of the circular implantation sites. d) The atomic force microscopy image from (c) shows the selected implantation site as 3D topography map. The irradiated region localized by the aperture is highlighted by a white dashed circle. Lithographic alignment markers mapped by the AFM cantilever (not shown here) allow non-invasive nanometer precision alignment between ion implant sites and subsequent device processing steps.

shallow ion implantation (Figure 2c). These sites allow the subsequent construction of multiple many-donor devices on a single chip (Figure 2d). Each site has a lateral diameter

© 2021 The Authors. Advanced Materials published by Wiley-VCH GmbH

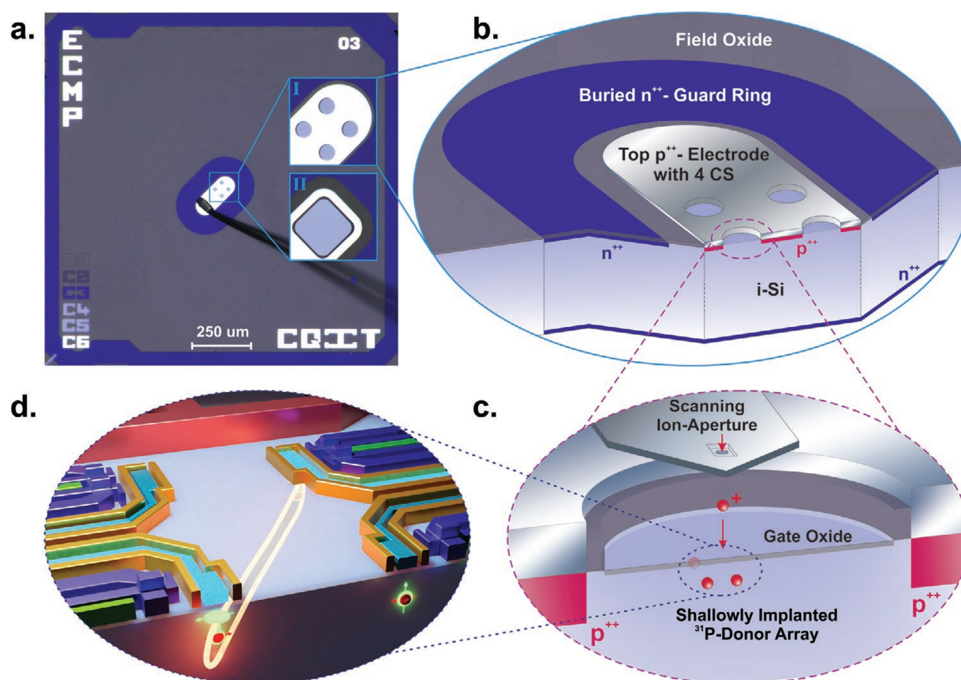

Figure 2. Localization of single-ion implants. a) Optical top-view microscopy image of a single-ion detector chip. Two different construction site (CS) designs are available for the present study. The first comprises four separated circular CS (configuration I) with each 20 µm diameter and the second comprises a single larger rectangular CS (conFigure II) with dimensions 60 × 60 µm². b) Cross-sectional schematic of the silicon single-ion detector chip incorporating a vertical p–i–n geometry. The detector incorporates a top electrode surrounded by a floating n-type guard ring to minimize leakage current. The construction sites surface layer is a uniform 6 nm thin thermal SiO_2 gate oxide on the intrinsic (100) silicon substrate. c) Shows the concept of formation of a donor array by deterministic step-and-repeat single-ion implantation in the selected construction site. The AFM cantilever, which incorporates a nanostencil aperture, acts as a movable mask for the ion beam. The signal from a single-ion implant event triggers the AFM nanostencil scanner to step to the next implant site. d) Schematic of a 2 × 2 ^{31}P-donor array with ≈200 nm spacing, as appropriate for flip-flop qubit devices.[40] These qubits employ long-range electric dipole interactions (depicted by the yellow loop), so that entangling gate operations can be performed even beyond the nearest-neighbours, for instance across the diagonal of the array as shown. The control and readout circuitry is fabricated after the implantation and the rapid thermal anneal required for donor activation.

of 20 µm, providing real estate for up to 10^4 donors when arranged in a flip-flop-qubit layout as exemplified in Figure 2d. A rectangular 60 × 60 µm² construction site configuration II (see Figure 2a) can host arrays of up to 10^5 implanted donors and is also sufficiently sized for mid-term donor qubit entanglement studies on mesoscale arrays. As shown in Figure 2b, the construction sites are surrounded by a detector top electrode, and each site features a pre-fabricated thin gate oxide needed for subsequent integration of donor control nanocircuitry on the surface. The top electrode makes contact with a boron-doped p-well on the intrinsic silicon substrate, with an n-type back contact forming the p–i–n detector. To meet the low noise performance requirements, two important design features are employed: i) A floating buried n-type guard ring surrounds the top electrode and screens the active detector volume against parasitic free charge carriers from outer interface and bulk defects[46] and minimizes the reverse bias leakage current, which would otherwise obscure ion impact signals; ii) minimized area top electrode to lower the total device capacitance and consequently the parallel white noise contribution in the charge-sensitive preamplifier.

The principle of controlled donor array formation inside a selected construction site is illustrated in Figure 2c. An AFM nanostencil scanner localizes the implant site to high spatial precision and steps to the next array site when triggered by the ion implant signal from the detector electrodes. The signal can also trigger a fast ion beam blanker (typically ≈100 ns response time) to minimize the probability of further implant events at the same array site.

The gate dielectric in each construction site is a 6 nm-thin high-quality thermally grown SiO_2 oxide (see Section 8) made in advance of all other fabrication steps because the high-temperature process would otherwise cause an unacceptably large diffusion of implanted donors. Moreover, the thermal growth of the gate oxide has the advantage of passivating interface charge traps and reducing fixed oxide charges that would otherwise trap and reduce the ion-induced charge signal in the detector. The ions traversing the gate oxide during implantation suffer from some kinetic energy loss that is not available for the signal generation. However, this effect is tolerable given the low oxide thickness and the excellent signal detection efficiency enabled by this surface passivation.

Defect densities associated with the gate oxide are critical parameters for the function of devices in our material. Measured densities are obtaind from metal-oxide-semiconductor capacitor (MOSCap) devices, processed together with the detector wafers. The results are ≤2 × 10^{10} eV^{-1} cm^{-2} for the oxide interface trap density and ≤2 × 10^{11} cm^{-2} for the fixed oxide charge density. The trapping of single-ion-induced charge by these defects is negligible. This ensures close to 100% of

© 2021 The Authors. Advanced Materials published by Wiley-VCH GmbH

the charge contributes to the signal at implantation energies of interest. In the broader context of our applications, these low trap densities also indicate that the material is suitable for practical high-fidelity operation of donor qubits.[10] Earlier studies showed that similarly low values of trap densities are retained after ion implantation, followed by a high-temperature rapid thermal anneal and a forming gas anneal.[47] The high quality of post-implantation oxides is further corroborated by the robust charge and spin properties of qubit devices based on ion-implanted donors as studied in the past decade[10–16,26,48]

4. Detection of Induced Charge Signals

To detect the signal from ≲1000 e–h pairs induced by a single-ion implant with high confidence requires a minimization of the noise generated by the detector and associated electronics. The noise performance of a solid-state detector is mainly determined by the combined leakage current I_{tot} and capacitance C_{tot} of the detector and its first-stage amplifier. For ultralow noise applications, the latter typically consists of a junction field-effect transistor (JFET), whose internal gate design and fabrication technology[49,50] determine I_{tot} and C_{tot}.

Our system incorporates several optimization strategies developed for different applications. State-of-the-art radiation detectors for X-rays feature an integrated JFET and exhibit a capacitance on the order of $C_{tot} \leq 300$ fF.[51] Fast-recovery p–i–n photo diodes can have a full-depletion reversed bias leakage current as low as $I_{tot} \leq 1$ pA at room temperature.[52] These highly application-optimized detectors provide a benchmark for the performance of our detectors optimized for deterministic doping. **Figure 3**a illustrates capacitance–voltage (*C*–*V*) and current–voltage (*I*–*V*) graphs representative of the present detector alongside results from a reference photodiode.[52] By minimizing the top electrode area that contains the construction sites, and incorporating an n-guard ring surrounding the top electrode to suppress leakage current, we obtained a capacitance of 80 ± 30 fF (a factor four lower than the reference diode) and a leakage current of approximately 35 ± 10 pA at 10 V reverse bias and room temperature operation. Moderate cooling to 263 K (–10 °C) reduces leakage to the required sub-pA regime. Improvement of these values is expected by further optimization of the detector fabrication process.

Non-destructive experimental measurements of the detector noise are obtained using a ^{57}Co calibration radionuclide, emitting characteristic Fe K_α and K_β X-ray photons at 6.40 keV and 7.06 keV, respectively. Upon absorption inside the active detector volume, an X-ray photon excites a number of e–h pairs proportional to its energy. In general, the excitation of one e–h pair requires $\varepsilon_{Si} = 3.6$ eV of energy in silicon. Drift of these e–h pairs in the bias field results in a charge-equivalent voltage pulse q at the detector electrodes, whose amplitude in units of volts is determined by the feedback capacitance $C_F = 50$ fF of our charge-sensitive pre-amplifier circuit. The measured pulse amplitude q is in turn proportional to the photon energy $E_{X\text{-ray}}$ and commonly expressed in units of keV, with the conversion rule $q[\text{eV}] = q[\text{V}] \times C_F \times \varepsilon_{Si}/e$ and the elementary charge e. The signal spectrum, $s_{X\text{-ray}}(q)$, also features Bremsstrahlung background and detector noise.

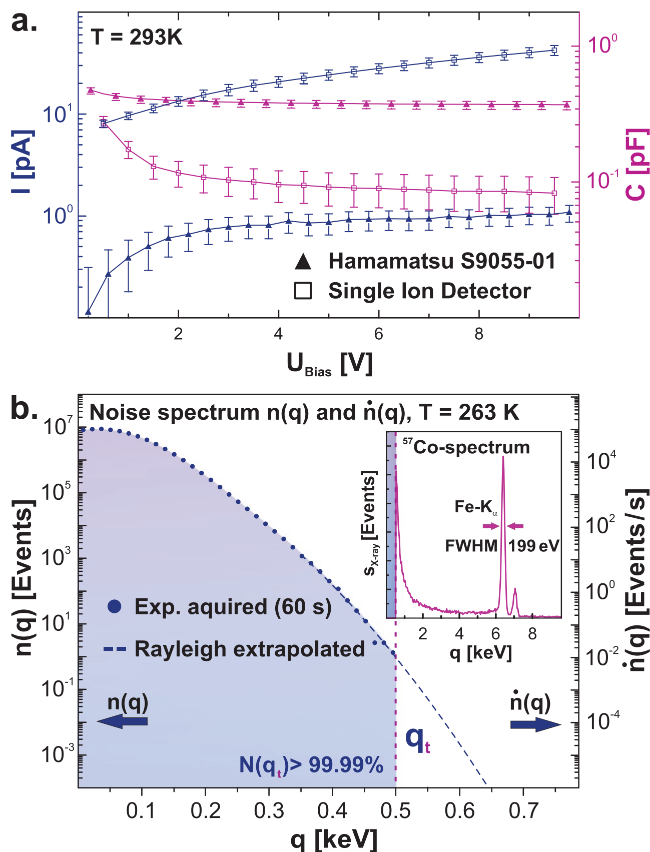

Figure 3. Detector characteristics. a) *I*–*V* and *C*–*V* data of our detector compared to a reference photodiode. The detector has a comparable low capacitance but a leakage current an order of magnitude higher, suggesting further improvements are possible. b) With the ion beam blanked, the detector dark noise spectrum $n(q)$ was acquired to a high statistical precision and is plotted as function of the charge-equivalent signal amplitude q (see text). The right vertical axis expresses the spectrum normalized as noise rate $\dot{n}(q)$ in [Events s^{-1}]. A Rayleigh distribution is used to extrapolate the noise spectrum for much longer acquisition times. A threshold q_t is delineated here, where better than 99.99% of the cumulative noise $N(q_t)$ (blue area) is discarded by a lower-level discriminator in the data acquisition electronics. The inset shows the ^{55}Fe X-ray K-emission lines of a ^{57}Co radionuclide, acquired with all system components activated, including the AFM itself. A resolution of about 200 eV FWHM for the 6.4 keV K_α peak acquired at a substrate temperature of 263 K verifies negligible signal degradation from cross-talk from the AFM system. This signal spectrum $s(q)$ also allows a quantitative calibration of the charge-equivalent signal axis q in units of [keV].

A representative X-ray spectrum from a present detector, operated at 263 K, is shown as inset in Figure 3b. The closely spaced Fe-K_α and K_β photon energies are clearly resolved. The K_α-peak exhibits an FWHM of about 200 eV, which corresponds to a root-mean-square (r.m.s.) noise of $\sigma_{noise} \approx 70$ eV and thus comparable to state-of-the-art silicon detectors for applications to X-ray spectrometry. The detector dark noise spectrum, $n(q)$, obtained at 263 K detector temperature and with no radionuclide present is shown in Figure 3b. As demonstrated in the following, the steep noise attenuation as a function of energy of ≈2.3 dB per 100 eV is essential for low energy single-ion detection with high confidence.

© 2021 The Authors. Advanced Materials published by Wiley-VCH GmbH

5. Deterministic Ion Implantation

The stopping of an ion as it dissipates kinetic energy in a crystal is caused by nuclear and electronic energy loss[53,54] in proportions that depend on the ion mass and energy as well as the solid material. The electronic stopping fraction $f_{el,i}$ of a single ion generates a proportional number of e–h pairs and thus an energy-equivalent charge signal pulse of amplitude q_i, which is utilized for the event detection. For an ensemble $\{i\}$ of consecutive ion implants, each event i contributes to a signal spectrum $s(q) = \{q_i\}$. Electron–hole (e–h) pairs generated within the gate oxide (i.e., outside the silicon crystal) and losses from charge recombination reduce the signal amplitude q_i. Further effects like ion channeling and substrate atom recoils influence the electronic fraction $f_{el,i}$ itself. The interaction of these factors leads to characteristic high and low energy tails in the spectrum $s(q)$, which consequently reflects both the stopping physics specific for an ion species as well as the detector properties.

To measure the response of the present detector to ion implantation, the AFM cantilever with a 16 µm-diameter aperture was used to localize the ion beam to the construction sites. We first show a spectrum from 14 keV H_2^+ ions. This molecular ion dissociates upon impacting the surface gate oxide, yielding two 7 keV H^+ ions, each having ≈100 nm average penetration depth. The e–h pairs produced by both ions induce a combined signal pulse in the detector. The low mass of protons results in ~95% of their kinetic energy dissipating in e–h-pair generation.[53,54] The signal spectrum (**Figure 4** inset) $s(q)$ thus exhibits a sharp peak at an energy very close to the 14 keV energy of the incoming H_2^+ ions. This result demonstrates the expected detector performance and negligible losses due to charge trapping and recombination. Furthermore, essentially no low energy signal events are registered outside the main peak body, indicating minimal scattering artifacts from the aperture in the cantilever used to collimate the ion beam in the detector construction site.

The four construction sites were subsequently irradiated with 14 keV P^+ ions until each of the corresponding signal spectra consisted of 5000 detected events, as illustrated in Figure 4. Note that a flip-flop qubit prototype device as per Figure 2c typically requires an inter-donor pitch of about 200 nm. This pitch leads to an average surface doping density of 25 atoms µm^{-2}, which is reflected in the areal density produced with the present implant parameters.

The intended application of our system is for controlled near-surface doping, particularly with the 14 keV P^+-ion implants presented here. The corresponding spectra, shown in Figure 4, exhibit a peak center at about 3.8 keV. Compared to the much lighter H_2^+ ions, this is significantly less than the incident ion kinetic energy, owing to the smaller fraction of electronic energy loss that generates e–h pairs. Also, the straggling from statistical variations in the ion stopping process leads to a more pronounced variation in the fraction of electronic energy loss compared to an ensemble of H_2^+ ions. Consequently, the P^+-ion signal spectrum is broader and ion channeling events, mainly along the Si [100] axis, exhibit an enhanced electronic

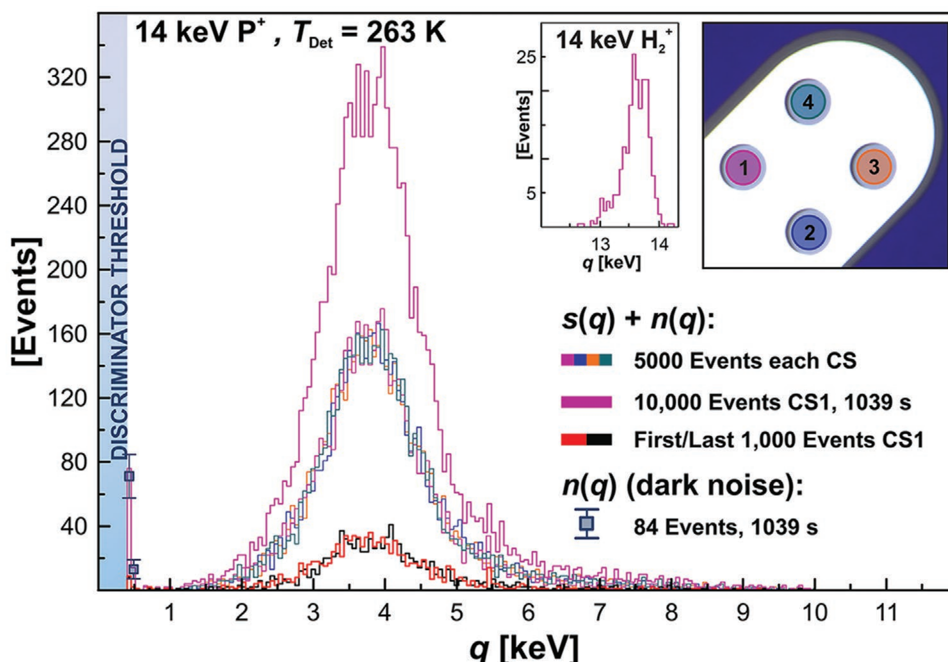

Figure 4. Counted ion implantation experiments: Experimental signal spectra $s(q) + n(q)$ of 14 keV P^+-ions implanted in four construction sites (CS) of the employed single-ion detector (as shown in the upper right optical image). Each of the four CS spectra contains 5000 signal events. The upper center inset shows an experimental spectrum for 14 keV H_2^+ molecule-ion implants (614 Events). These light ions with a high electronic stopping fraction confirm 100% charge collection efficiency of the detector. The channel-to-charge calibration of the q-axis was initially done using a ^{57}Co radionuclide. Construction site 1 was exposed to the ion beam to acquire 10 000 signal events $s(q) + n(q)$ over a period of 1,039 s and with the discriminator threshold reduced to $q_t = 0.4$ keV. The two sub-spectra of the first and last 1000 detected events, respectively, are shown as well and demonstrate negligible signal deterioration. Additionally, the dark noise spectrum $n(q \geq 0.4$ keV) is shown with the ion beam blanked-off and acquired for the same duration.

© 2021 The Authors. Advanced Materials published by Wiley-VCH GmbH

energy loss leading to a long high-energy tail up to 10 keV in the signal spectrum.

Notable is the close similarity of all four spectra in Figure 4, underpinning a spatially highly uniform gate oxide quality and reliable detection performance across larger implantation areas.

A selected construction site was subjected to about 5000 additional ion implant events, giving a signal spectrum composed of 10 000 detection events. Figure 4 highlights the spectrum $s(q) + n(q)$ whose acquisition time amounts to 1039 s (and thus about 9.5 Ions/s beam current). Also shown are two sub-spectra of the first and last detected 1000 events, respectively. Within the statistical limitations, these two sub-spectra do not differ regarding peak center position and full-width-at-half-maximum. This finding yields evidence that the crystal lattice damage accumulation even at an ion fluence twice the application-relevant value does not cause a measurable deterioration of the detector's charge collection efficiency. The signal spectrum thus reflects the ion–solid interaction physics in a pristine silicon crystal for these fluences.

For the given experimental data acquisition time of 1039 s, the confidence that a signal arises from a single-ion implantation event is limited by the probability that a noise event occurs within the same time window and signal amplitude. A discriminator threshold q_t is typically used to discard most of the low-energy events which are dominated by noise signals. To demonstrate the role of the discriminator threshold, the experimental spectrum $s(q) + n(q)$ of 10 000 signal events in Figure 4 was obtained with $q_t = 0.40$ keV (blue-coloured area) so that some signal events above that value, otherwise rejected by the optimum discriminator threshold (see next section), are retained in this exemplary signal spectrum. Additionally, the dark noise spectrum $n(q)$ in Figure 4, with the ^{31}P ion beam blanked-off, was acquired for the same time duration and threshold setting. We now examine the two experimental noise $n(q)$ and signal $s(q) + n(q)$ spectra in detail.

First, we consider the few dark noise signal events registered immediately above the discriminator threshold. Only the first two energy bins $q \in (0.40, 0.46]$ keV and $q \in (0.46, 0.51]$ keV contain 71 ± 17 and 13 ± 8 noise events, respectively, whereas each uncertainty is governed by noise events occurring randomly in time ($2\sqrt{\sigma(Events)}$ for a 95% confidence interval). In comparison, the experimental spectrum $s(q) + n(q)$, comprising 10 000 signal events in total, contains 76 and 14 events in both respective bins. This lies well within the uncertainty of obtained dark noise events and makes them all likely (but not certainly) caused by noise as well. Furthermore, no signal events were registered in the next two higher bins $q \in [0.51, 0.63]$ keV. Since the occurrence rate of dark noise events in the subsequent bin window $q \in (0.63, 0.69]$ is already vastly suppressed by three orders of magnitude (see previous section and Figure 3b), the solitary signal event registered therein can be ascribed to a real ^{31}P-ion implant event with a confidence of about 99.9%. The value also represents the lower ensemble confidence limit for the remaining set of 9910 signal events detected above 0.63 keV.

Consequently, the ion detection confidence from all 10 000 experimentally detected signal events in spectrum $s(q) + n(q)$ is predominantly governed by the uncertainty of the events stored in the two first bins above the discriminator threshold ($2\sqrt{76} + 2\sqrt{14} \approx 25 \pm 10$). Even without detailed signal analysis and modelling, the sufficient statistics allows a direct estimate that ≥99.75 ± 0.10% of the data set is not due to noise. By optimizing the discriminator threshold (as discussed below) this improves to 99.85 ± 0.02%.

6. Single-Ion-Detection Confidence

We now consider the implications of the experimental spectrum for the use of deterministic large-scale donor array fabrication. We determine the detection confidence by distinguishing the ion-induced signal spectrum $s(q)$ from the noise spectrum $n(q)$. This is achieved by combining an established physics modeling code with realistic experimental parameters to model $s(q)$. The trajectories of individual ions from straggling can be modeled to provide insights into the final location of the ion in the substrate and the corresponding signal amplitude from the detector.

We consider here a binary collision model for the ion–solid interaction to compute the associated electronic energy loss and hence the detector signal. The approach first uses the TRIM code to compute the ion trajectory through the surface gate oxide and to determine ion position and velocity vector at the interface to the silicon substrate (including recoiling Si and O atoms). Then, a modified Crystal-TRIM code is used to compute the ion trajectory inside the (100) oriented silicon crystal substrate and determine the total electronic energy loss of the ion and associated recoils. Details of the simulation procedure are explained in Section 8.

The result from this direct model to compute the signal spectrum of 99 100 virtual 14 keV $^{31}P^{+}$-ions is shown in **Figure 5**a. The simulation—downscaled by a factor of 10 to normalize to the ≈9910 experimentally detected ion implant events—agrees well with the experimental spectrum within Poisson statistics. It thus adequately models the various ion–solid interaction physics including ion channeling. This satisfactory match across the entire signal spectrum regime justifies the use of the simulation procedure to assess the single-ion-detection confidence for our experiments with 14 keV P^{+}-ions by examining the modeled trajectories.

We therefore evaluate this confidence by considering all relevant ion implant signals that are gathered or discarded by the detector system. Due to the partial overlap of the signal $s(q)$ and noise $n(q)$ distributions, it is possible to identify the optimum discriminator threshold level q_t by taking two critical quantities into account: false-positive signals from retaining noise above q_t, and false-negative signals from discarding ion implantation events below q_t. The false-positive rate is easily obtained by integrating the experimental noise spectrum $n(q)$ normalized to the acquisition time from q_t to ∞, i.e. $F_{\mathrm{Pos}}(q_t) := \dot{N}\,|_{q_t}^{\infty}$. The false-negative rate $F_{\mathrm{Neg}}(q_t) := \dot{S}\,|_{0}^{q_t}$ is derived via integration of the Crystal-TRIM model signal spectrum $s(q)$ and a normalization to the average ion incidence rate $r_{\mathrm{Ion}} = \dot{S}\,|_{0}^{\infty}$.

Figure 5b illustrates the experimentally obtained $F_{\mathrm{Pos}}(q_t)$ event rate as well as the $F_{\mathrm{Neg}}(q_t)$ event rate for an ion rate of $r_{\mathrm{Ion}} = 9.5\ \mathrm{s}^{-1}$ (as adopted from the experiment in Figure 4).

The ion detection confidence Ξ (normalized as probability) can be then derived as (see Section 8):

© 2021 The Authors. Advanced Materials published by Wiley-VCH GmbH

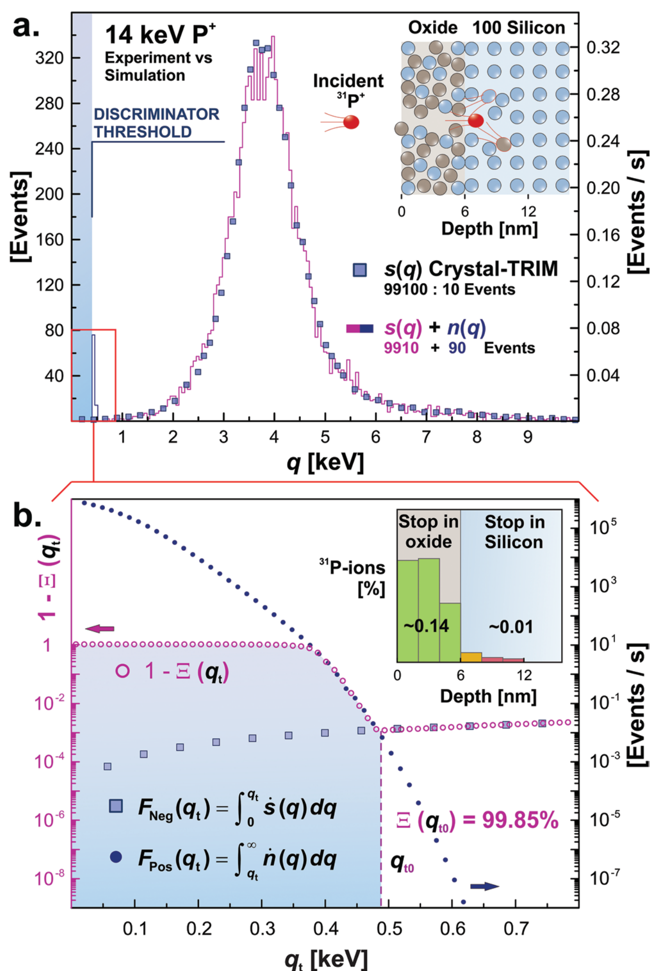

Figure 5. Counted ion implantation—analysis. a) The experimental signal spectrum of construction site 1 (see Figure 4) is plotted alongside a computed signal spectrum using the Crystal-TRIM code. The upper-right inset illustrates the sample geometry for the simulation. The simulation package considers the collision cascades inside the (100) oriented silicon crystal substrate from the primary $^{31}P^{+}$ ion as well as forward-recoiled gate oxide Si and O atoms. b) The cumulative "false positives" F_{Pos} and "false negatives" F_{Neg} are plotted alongside the single-ion-detection diffidence $1 - \Xi$ as a function of the discriminator threshold level q_t. The optimum value q_{t0} yields a nominal detection confidence of 99.85% for the given ion implantation rate in this experiment. The upper right inset depicts the placement depths of $^{31}P^{+}$ ions that cause non-detectable (missed) sub-threshold signal events $F_{Neg}(q_t)$. The majority consists of non-critical donors that stop in the surface gate oxide.

$$\Xi(q_{t0}) = \left(1 - \frac{F_{Neg}(q_{t0})}{r_{Ion}}\right)\left(\frac{r_{Ion}}{r_{Ion} + F_{Pos}(q_{t0})}\right) \tag{1}$$

with the first factor describing the fraction of ions that create detectable signal events above the optimum threshold level q_{t0} and the second factor stating the probability that the registered event was not due to noise. Equation (1) constitutes an optimization problem with the threshold level q_{t0} adjusted to maximize Ξ. For comprehensibility reasons, the single-ion-detection diffidence $1 - \Xi$ is illustrated in Figure 5b. For q_t set to a very low threshold level, false positives F_{Pos} dominate the acquired signal and cause the diffidence to saturate to 1 (or zero detection confidence). At the other extreme, for q_t set to a high threshold level, false negatives (rejected real ion implantation signals) F_{Neg}g become the main confidence limitation. Noteworthy in Figure 5b. is the shallow curve profile of F_{Neg} throughout the entire sub-threshold signal range, limiting the detection confidence Ξ to <99.99%. This is owing to rare collision cascades in the gate oxide, governed by the physics of the ion–solid interaction.

The actual experimental detection confidence is also governed by the optimum threshold level, determined from the data in Figure 5b. It is found to be $q_{t0} \approx 0.49$ keV, yielding a single-ion-detection confidence of $\Xi(q_{t0}) = 99.85 \pm 0.02\%$. This result is a very weak function of the statistics in the signal spectrum, because the numerical models of $n(q)$ and $s(q)$ are fitted to statistically sound experimental signal spectra with high confidence.

Our computational model allows us to assess the ≈0.15% implant events that produce signals below the optimum discriminator threshold (i.e. missed events). As tabulated in the inset of Figure 5b, the model shows that most of these ions (0.14% of total) stop inside the surface gate oxide or, rarely (<0.01% of total), backscatter from the sample surface. Only the residual (0.01% of total) of ions end up in the silicon substrate without producing a signal above the threshold. These 0.01% of implant sites will therefore contain two implanted atoms, or a single double-implant site out of 9910 for our experimental configuration.

However, it must be stressed that the single-ion-detection confidence, as defined in Equation (1), models signals of ion implant events and therefore represents the upper-bound to the controlled silicon doping yield. For our application, the conversion of the implanted ion into a donor qubit requires consideration of additional materials engineering factors, such as the donor activation yield (≈100% for ^{31}P as discussed in introduction) as well as the donor placement constraints imposed by the device architecture. For example, the substrate of the present devices incorporates a prefabricated low defect density 6 nm surface gate oxide. As explained earlier, this engineering constraint is imposed because the oxide thermal growth budget would cause unacceptable donor diffusion if fabricated post-implantation. For this architecture configuration our model predicts ≈1.9% of ions stopping in the gate oxide also induce a signal above the optimum discriminator threshold, owing to forward recoil atoms that enter the silicon substrate. In our devices, Si forward recoils are of minimal concern and O forward recoils are highly mobile in silicon. Post-implant annealing, even at temperatures below 500 °C, drives the O recoils to bond to the gate oxide interface or diffuses them deep into the large substrate volume. Therefore, the most likely result from these events is a vacant site without yielding a useful dopant atom. In general, there are additional materials engineering factors such as deep straggling owing to ion channeling, where the donors may be in unsuitable locations for surface gate control. Our model predicts that improvement of the present 6 nm gate oxide to state-of-the-art 3 nm reduces the fraction of 14 keV ^{31}P ions stopping in the gate oxide from 1.9% to 0.3%. Ultrathin gate oxides and post-implant fabricated gate stacks have the further advantage that the implant energy can be reduced to further diminish straggling, without sacrificing

© 2021 The Authors. Advanced Materials published by Wiley-VCH GmbH

ion energy in the oxide dead layer that would otherwise diminish the single-ion implant signal. Heavy dopants, such as ^{123}Sb and ^{209}Bi, will have a negligible vacant site fraction due to reduced spatial implantation straggling. These materials engineering advances will allow the controlled silicon doping yield approaching the confidence limit defined by Equation (1).

7. Conclusion

We have presented an advanced single-ion implantation system incorporating an AFM-based aperture scanner and operating near room-temperature. It allows configuration of substrate material, in this case silicon, with counted numbers of dopants by deterministic ion implantation employing signals from ion-induced e–h pairs inside the electrically active silicon substrate. The system can be employed to implant near-surface donor arrays for applications including single-atom spin qubit devices such as the 2D architectures exploiting the flip-flop-qubit.[40] Our single-ion detector electronics exhibits an exceptionally low noise background at near-room temperature, as shown with 14 keV $^{31}P^{+}$-ions. The system is compatible with many standard ion implanters, commonly equipped with stochastic ion sources that cause random ion arrival times at the substrate. The detector signals from implanted ions provide a characteristic spectrum that allows deeper insight into the ion–solid interaction. The physical model provides insights into the rare implantation events that produce sub-threshold ion signals.

For the configuration of our system, we conclude that the confidence of detecting a single-ion implantation event into our device has the physical upper-bound of 99.85%, with a materials engineering constraint of 98.1% owing to 1.9% of the detected 14 keV $^{31}P^{+}$-ions stopping in the 6 nm gate oxide. Remarkably, the residual detection diffidence $1 - \Xi(q_t 0) = 0.15\%$ can be mainly attributed to the stopping physics of 14 keV $^{31}P^{+}$-ions in silicon, whereas the detector noise plays only a subordinate role. Hence, our strategy enables controlled dopant implantation at the physical limit in accord with the physics model of the ion–solid interaction. Future studies will analyse advanced scalability projections for 2D donor array formation and extend Equation (1) to include the double-implant probability as a function of the incident ion beam current (see Section 8). These considerations will become important when seeking to increase the ion beam fluence to reduce the total implantation time for large donor arrays.

In summary, our results show that a single 14 keV $^{31}P^{+}$-ion, implanted in a silicon device operated at near-room temperature and integrated with an AFM aperture scanner, can be detected with extremely high confidence. Therefore, single-ion detection uncertainties will not constitute an obstacle to the construction of a fault-tolerant, large-scale donor-based quantum computer in silicon. The present devices incorporate multiple construction sites on one chip to mitigate engineering factors that cause device variations and also allow the investigation of device architecture parameter optimization. Counted single- and multi-atom devices as well as independent assessment methods are presently being prepared and tested for this purpose.

8. Experimental Section

Detector Fabrication: Standard metal–oxide–semiconductor (MOS) processing[55] is employed to fabricate the detectors studied in this work. The initial wafer is a ⟨100⟩ Uniform High Purity Silicon (UHPS) wafer from Topsil. The low residual n-doping yields a resistivity of 9250 Ω cm. The on-chip single-ion detectors are fabricated as follow:

1) Etching of alignment markers for subsequent optical lithographical steps: The pattern is first defined using standard optical lithography and then transferred into a previously grown wet thermal SiO_2 oxide. Using tetramethylammonium hydroxide (TMAH), the pattern is then etched into the silicon; the oxide is subsequently removed using BHF.
2) Creation of the detector's p-doped regions: The area to be doped is defined using standard optical lithography and then transferred onto a thermally-grown wet oxide. P-type doping is obtained by thermal diffusion of boron. Lastly, the oxide is removed using BHF.
3) Back n-doping of the detector: first, a thermal oxide is grown in a steam ambient. Using photoresist as a mask, the oxide on the back of the detector is then removed using BHF. This then serves as the mask for the thermal diffusion doping of the rear of the detectors using phosphorous. The masking oxide is then removed using BHF.
4) Growth of the thick field oxide using a dry oxidation process.
5) Growth of the thin gate oxide using a dry oxidation process, in areas defined within the field oxide using optical lithography and etched using BHF.
6) Etching of vias for metallization using a photolithographic mask and BHF.
7) Deposition of metallization: A mask is first defined using photolithography and any native oxide that has grown onto exposed silicon is removed using a quick hydrofluoric acid dip. Using e-beam evaporation, 100 nm of aluminium is then deposited onto the wafer, directly followed by 10 nm of platinum, both on the front and back. Metallization in undesired regions is removed using a lift-off process using warm *N*-methyl-2-pyrrolidone (NMP).
8) Annealing of the detectors in a forming gas ambient (5% hydrogen, 95% nitrogen) at 400 °C.

I–V/C–V Analysis: Detector chips are mounted on a chip carrier and placed inside a light-shielded analysis chamber held under rough vacuum ($\approx 1 \times 10^{-3}$ Torr). The chip carrier is attached to a low-noise multiplexed feedthrough that allows interconnection to either a Keithley 6487 picoammeter (resolution 20 fA) or Boonton 7200 capacitance meter (resolution 1 fF) for *I–V* and *C–V* measurements, respectively.

FOC/DIT Analysis: The Si/SiO_2 interface trap densities (Dit) were estimated using the Hill-Coleman method and deep level transient spectroscopy. Mid-gap values of test devices with a 5 nm oxide are found to be in the low 10^{10} cm^{-2} eV^{-1} range. The fixed oxide charge was estimated by identifying the flat band voltage shift in a CV curve as a function of oxide thickness. Values are in the low 10^{11} cm^{-2} range.

Charge-Sensitive Electronics: The charge-sensitive preamplifier printed circuit board is based on the forward-biased FET design of Bertuccio et al.[41] and incorporates a commercial miniaturized thermo-electrical-cooling element that hosts the single-ion- detector chip and the separate JFET die (with the JFET selected for its gate matching the detector capacitance and exhibiting low forward bias gate-source leakage current). Electric connection between detector, JFET and preamplifier board is established via wire bonds. The preamplified signal pulse is fed into an Amptek PX5 digital pulse processor, which performs trapezoidal pulse shaping ($\tau_{peak} = 9.6$ µs) and multi-channel analysis to provide the final signal histogram data via USB connection to the Amptek MCA control- and acquisition software.

Additionally, the digital signal resolution was set to about 57 eV per channel (256 channels ranging from 0 to 14.6 keV) to give about 6% statistical variation in the maximum counts per channel for the total fluence of 10 000 ion counts. This choice is also consistent with the ion energy straggling which does not justify a higher resolution.

© 2021 The Authors. Advanced Materials published by Wiley-VCH GmbH

Nanostencil Fabrication: The fabrication of the aperture in the AFM cantilever to form the nanostencil is done with an FEI Scios SEM/FIB system. The aperture can be made with a diameter from microns down to sub-10 nm via in situ monitoring with the SEM. After milling the aperture a Pt layer of 50 nm thickness is deposited in-situ on both entry and exit openings of the aperture which reduces the probability of forward scattered ions reaching the substrate. The resulting channel length of the aperture in the ion direction is sub-500 nm. This measure lowers the interaction probability between passing ions and aperture walls, and consequently shallow-angle scattering effects. They can be caused by the intrinsic ion beam divergence of about 9 mrad along the aperture tunnel axis. The aperture position relative to the probe tip apex of the cantilever is measured from SEM imaging at the conclusion of the fabrication process. This lateral offset allows atomic force microscopy topographic images to be precisely aligned with the implant sites from ions passing through the aperture.

Ion Beamline and Detection Experiments: The raw P^+-ion beam is generated in a BIS DCIS-100 DC plasma filament using a gas intermix consisting of 5% PF_5 diluted in 95% Argon. A BIS 600-B Wien filter selects the ion species with a beam divergence of typically 9 mrad and about 10 nA beam current. The vacuum pressure inside the ion source chamber is 1×10^{-6} Torr and about 5×10^{-8} Torr in the beam line during operation. A commercial double V-slit configuration made of tantalum membranes and attached to micro-meter screws is employed for beam current adjustment. Further ion beam purification and removal of scattered vacuum background atoms is realized via an NEC 90° electrostatic spherical dipole analyser located at the target chamber entry. A Tungsten membrane of 25 µm thickness and 20 µm aperture diameter pre-collimates the ion beam onto the AFM nanostencil aperture. Precision ion current adjustment to 9.5 ions s^{-1}, respectively, was done on a sacrificial detector construction site by monitoring the ion signal rate.

A long working distance optical microscope provides a top view on the substrate via a 45° mirror with integrated ion aperture. It is used for coarse alignment between AFM nanostencil and ion beam spot as well as the detector relative to the nanostencil. The optical resolution is approximately 2 µm.

Theory: In order to produce a functional qubit via deterministic ion implantation, the following requirements have to be fulfilled: i) on each location exactly one ion is implanted with a yield defined to be Y_{DetIon}; ii) the final location of the ion in the matrix is compatible with the tolerances of the qubit architecture, which is constrained by the ion straggling and related yield Y_{QCon}; iii) the implanted ion is successfully activated upon thermal anneal with the yield Y_{Act}. The overall yield Y to form a functional donor qubit then is

$$Y = Y_{\mathrm{DetIon}} \cdot Y_{\mathrm{QCon}} \cdot Y_{\mathrm{Act}} \tag{2}$$

In the following, Y_{DetIon} is addressed for the experimental approach presented here and its derivation may differ for other approaches to deterministic ion implantation. In order to successfully record the implantation of an ion, the signal induced by the ion must exceed the data acquisition threshold q_{t0}. With $F_{\mathrm{Neg}}(q_{t0}) / r_{\mathrm{Ion}}$ as the fraction of ions that create signals below q_{t0}, the yield for $s(q) > q_{t0}$ is

$$Y_{s>q_{t0}}(q_{t0}) = 1 - F_{\mathrm{Neg}}(q_{t0}) / r_{\mathrm{Ion}} \tag{3}$$

Furthermore, the signal recorded above the threshold q_{t0} shall not be due to noise events that are erroneously interpreted as an ion implant event. The probability that the signal above q_{t0} is related to noise is given as the fraction

$$F_{\mathrm{Pos}}(q_{t0}) / (F_{\mathrm{Pos}}(q_{t0}) + r_{\mathrm{Ion}}) \tag{4}$$

Hence, the yield $Y_{\mathrm{NoNoise}}(q_{t0})$ that the signal above q_{t0} is not due to noise is

$$Y_{\mathrm{NoNoise}}(q_{t0}) = 1 - F_{\mathrm{Pos}}(q_{t0}) / (F_{\mathrm{Pos}}(q_{t0}) + r_{\mathrm{Ion}}) = r_{\mathrm{Ion}} / (F_{\mathrm{Pos}}(q_{t0}) + r_{\mathrm{Ion}}) \tag{5}$$

The ion beam from the nanostencil dwells on an implant site until a signal above q_{t0} is recorded. Then the beam is blanked off to protect the implant site from further ion implants and for the nanostencil to re-position to the next implant site. The beam blanker duty cycle time depends on parameters including the signal rise time in the pre-amplifier and related blanker trigger electronics as well as the charging time of the beam electrostatic deflector plates. Realistically achievable blanker times are $\tau = 100$ ns. Since the ion source delivers the ions stochastically in time, there is a probability P_{DI} that a second ion is implanted, creating an unwanted double implant. The probability $\mathrm{PDI}(\tau, r_{\mathrm{Ion}})$ is given by $e^{-\tau r_{\mathrm{Ion}}}$. Hence, the yield that no double implant occurs is $1 - P_{\mathrm{DI}}$. The yield of successful deterministic ion implants is then given by

$$Y_{\mathrm{DetIon}}(q_{t0}, \tau) = Y_{s>q_{t0}}(q_{t0}) \cdot Y_{\mathrm{NoNoise}}(q_{t0}) \cdot (1 - P_{\mathrm{DI}}(\tau, r_{\mathrm{Ion}})) \tag{6}$$

Due to the low ion rate on the order of 10 s^{-1} and all ions being implanted in one site (only one blanking cycle at the start and end of experiment) for the experiment presented above, the double implant probability is of the order of $P_{\mathrm{DI}} \approx 10^{-6}$ and has therefore been neglected in Equation (1), which then reduces to

$$Y_{\mathrm{DetIon}}(q_{t0}) \approx \Xi(q_{t0}) = Y_{s>q_{t0}}(q_{t0}) \cdot Y_{\mathrm{NoNoise}}(q_{t0}) \tag{7}$$

Simulations: The simulation of the signal spectrum consists of two steps. At first, the TRIM code[56] is applied to treat the P^+ ion transmission through the thin amorphous silicon oxide layer representing the surface gate oxide on the devices. From this, it is possible to simulate the energies and directions of a population of P ions transmitted through the oxide layer and of the recoiled Si and O atoms which are directed into the underlying (100) Si. In the second step, the code Crystal-TRIM[57–59] is employed to obtain the electronic energy loss per P ion in the population within the underlying Si. This quantity corresponds to the signal measured by the detector. Finally, detector noise and Fano statistics of e–h-pair generation were taken into account and allow the direct comparison with the experimental signal spectrum (see Figure 4a). Crystal-TRIM simulates the trajectories of energetic projectiles (in the present case: P, Si and O) in single crystal Si and can therefore treat channeling effects that cause larger values of electronic energy loss per ion than in amorphous Si. Like TRIM, Crystal-TRIM is based on the binary collision approximation, which assumes that the motion of an energetic projectile may be described by a sequence of binary collisions with target atoms. The trajectory of a projectile between two subsequent collisions is approximated by a straight line given by the asymptote to the trajectory of the energetic particle after the first collision. The electronic energy loss occurring during the collision of a projectile with a target atom is described using a semi-empirical expression, depending on an impact-parameter and is similar to the Oen–Robinson model.[57,58,60] In the present work, the value 3.0 was chosen for the model parameter c_d in the case of P and 1.5 for the Si and O projectiles. The value of the second parameter c_λ was set to 0.935 for P and Si and to 1.8 for O. This parameter describes the average electronic energy loss for random incidence directions of a projectile. Therefore, $c\lambda$ determines the energy related to the histogram peak maximum of the electronic energy loss per incident P ion. The shape of the histogram is sensitive to the parameter c_d, which influences the channeling of a projectile. Thermal vibrations of lattice atoms affect projectile trajectories, especially for the motion in channels. In Crystal-TRIM a simple model is used to take into account this effect.[57] Only the motion of P, Si, and O projectiles in single-crystalline Si is followed. However, the Si recoils formed in the collision cascades of these projectiles also contribute to electronic energy loss per incident P ion. This contribution is described by the semi-empirical expression of Funsten et al.,[61,62] which considers non-negligible self-trapping mechanisms due to a high density of low-energy e–h pairs generated closely around the path of energetic ion projectiles. For the purpose of the present work, the Crystal-TRIM code was modified by the introduction of the Funsten model. This semi-empirial approach

 © 2021 The Authors. Advanced Materials published by Wiley-VCH GmbH

replaces earlier models that employed the model of Robinson.[63] Test calculations showed that the Robinson model is not capable to describe the electronic energy loss of the low-energy Si recoils to be treated in this work. To date, the code has been applied in more than 200 peer-reviewed publications since its first introduction in 1994. The model has been validated with experimental SIMS data sets of P-donor depth profiles from the literature.[64]

Acknowledgements

The authors thank F. E. Hudson and A. S. Dzurak for discussions and support in the establishment of this research project. The research at the University of Melbourne and UNSW was funded by the Australian Research Council Centre of Excellence for Quantum Computation and Communication Technology (Grant No. CE170100012) and the US Army Research Office (Contract No. W911NF-17-1-0200). The authors acknowledge a grant from the University of Melbourne Research and Infrastructure Fund (RIF) and use of the facilities of the Australian National Fabrication Facility (ANFF) at the Melbourne Centre for Nanofabrication (MCN) and at UNSW. S.G.R. and H.R.F. acknowledge the support of an Australian Government Research Training Program Scholarship. A.M.J. acknowledges an Australia–Germany Joint Research Cooperation Scheme (UA-DAAD) travel scholarship that supported collaboration with partner institutions in Germany. The authors are grateful to D. McCulloch of the RMIT Microscopy and Microanalysis Facility for use of SEM/FIB and TEM equipment. The views and conclusions contained in this document are those of the authors and should not be interpreted as representing the official policies, either expressed or implied, of the ARO or the US Government. The US Government is authorized to reproduce and distribute reprints for government purposes notwithstanding any copyright notation herein.

Conflict of Interest

The authors declare no conflict of interest.

Author Contributions

A.M.J. designed and constructed the detector preamplifier electronics and the integration of the ion beam line with the AFM nanostencil scanner. A.M.J. conceived and conducted the deterministic implantation experiments with assistance from S.G.R. A.M.J., V.S., V.M. and B.C.J. developed single-ion detectors. V.S., V.M. and H.R.F. fabricated single-ion detectors. S.G.R. and B.C.J. conducted DIT/FOC as well as *C–V*/*I–V* analysis for iterative detector performance improvement. S.G.R. performed FIB ion-aperture milling and SEM imaging, with assistance from E.M.; A.M.J. and D.S. developed theoretical groundwork on the detection confidence. M.P. developed the Crystal-TRIM code. A.M.J. and M.P. conducted Crystal-TRIM computations and analysis. J.C.M. contributed to the design of the ion implantation experiments. A.M. provided the design of the flip-flop qubit architecture, the design constraints on the fabrication of the detectors, and supervised the research at UNSW. D.N.J. conceived the deterministic ion implantation process and the implementation of the apparatus. The manuscript was written by A.M.J. and D.N.J. with contributions from the co-authors.

Data Availability Statement

The data that support the findings of this study are available from the corresponding author upon reasonable request.

Keywords

nanomaterials, nanotechnology, semiconductors, sensors

Received: April 28, 2021
Revised: August 17, 2021
Published online: November 12, 2021

[1] J. Preskill, *Quantum* **2018**, *2*, 79.
[2] F. Arute, K. Arya, R. Babbush, D. Bacon, J. C. Bardin, R. Barends, R. Biswas, S. Boixo, F. G. S. L. Brandao, D. A. Buell, B. Burkett, Y. Chen, J. Chen, B. Chiaro, R. Collins, W. Courtney, A. Dunsworth, E. Farhi, B. Foxen, A. Fowler, C. M. Gidney, M. Giustina, R. Graff, K. Guerin, S. Habegger, M. Harrigan, M. Hartmann, A. Ho, M. R. Hoffmann, T. Huang, T. S. Humble, S. V. Isakov, E. Jeffrey, Z. Jiang, D. Kafri, K. Kechedzhi, J. Kelly, P. V. Klimov, S. Knysh, A. Korotkov, F. Kostritsa, D. Landhuis, M. Lindmark, E. Lucero, D. Lyakh, S. Mandrà, J. R. McClean, M. McEwen, A. Megrant, X. Mi, K. Michielsen, M. Mohseni, J. Mutus, O. Naaman, M. Neeley, C. Neill, M. Y. Niu, E. Ostby, A. Petukhov, J. C. Platt, C. Quintana, E. G. Rieffel, P. Roushan, N. C. Rubin, D. Sank, K. J. Satzinger, V. Smelyanskiy, K. J. Sung, M. D. Trevithick, A. Vainsencher, B. Villalonga, T. White, Z. J. Yao, P. Yeh, A. Zalcman, H. Neven, J. M. Martinis, *Nature* **2019**, *574*, 505.
[3] A. G. Fowler, M. Mariantoni, J. M. Martinis, A. N. Cleland, *Phys. Rev. A* **2012**, *86*, 032324.
[4] L. Kranz, S. K. Gorman, B. Thorgrimsson, Y. He, D. Keith, J. G. Keizer, M. Y. Simmons, *Adv. Mater.* **2020**, *32*, 2070298.
[5] S. Nagayama, A. G. Fowler, D. Horsman, S. J. Devitt, R. V. Meter, *New J. Phys.* **2017**, *19*, 023050.
[6] J. M. Auger, H. Anwar, M. Gimeno-Segovia, T. M. Stace, D. E. Browne, *Phys. Rev. A* **2017**, *96*, 042316.
[7] K. Fischer, M. Agostinelli, C. Allen, D. Bahr, M. Bost, P. Charvat, V. Chikarmane, Q. Fu, C. Ganpule, M. Haran M. Heckscher, H. Hiramatsu, E. Hwang, P. Jain, I. Jin, R. Kasim, S. Kosaraju, K. S. Lee, H. Liu, R. McFadden, S. Nigam, R. Patel, C. Pelto, P. Plekhanov, M. Prince, C. Puls, S. Rajamani, D. Rao, P. Reese, A. Rosenbaum, S. Sivakumar, B. Song, M. Uncuer, S. Williams, M. Yang, P. Yashar, S. Natarajan, in *2015 IEEE Int. Interconnect Technology Conf. and 2015 IEEE Materials for Advanced Metallization Conf. (IITC/MAM)*, IEEE, Piscataway, NJ, USA **2015**, pp. 5–8, https://doi.org/10.1109/IITC-MAM.2015.7325600.
[8] F. A. Zwanenburg, A. S. Dzurak, A. Morello, M. Y. Simmons, L. C. Hollenberg, G. Klimeck, S. Rogge, S. N. Coppersmith, M. A. Eriksson, *Rev. Mod. Phys.* **2013**, *85*, 961.
[9] B. E. Kane, *Nature* **1998**, *393*, 133.
[10] J. J. Pla, K. Y. Tan, J. P. Dehollain, W. H. Lim, J. J. L. Morton, D. N. Jamieson, A. S. Dzurak, A. Morello, *Nature* **2012**, *489*, 541.
[11] J. J. Pla, K. Y. Tan, J. P. Dehollain, W. H. Lim, J. J. L. Morton, F. A. Zwanenburg, D. N. Jamieson, A. S. Dzurak, A. Morello, *Nature* **2013**, *496*, 334.
[12] J. T. Muhonen, J. P. Dehollain, A. Laucht, F. E. Hudson, R. Kalra, T. Sekiguchi, K. M. Itoh, D. N. Jamieson, J. C. McCallum, A. S. Dzurak, A. Morello, *Nat. Nanotechnol.* **2014**, *9*, 986.
[13] J. T. Muhonen, A. Laucht, S. Simmons, J. P. Dehollain, R. Kalra, F. E. Hudson, S. Freer, K. M. Itoh, D. N. Jamieson, J. C. McCallum, A. S. Dzurak, A. Morello, *J. Phys.: Condens. Matter* **2015**, *27*, 154205.
[14] J. P. Dehollain, J. T. Muhonen, R. Blume-Kohout, K. M. Rudinger, J. K. Gamble, E. Nielsen, A. Laucht, S. Simmons, R. Kalra, A. S. Dzurak, A. Morello, *New J. Phys.* **2016**, *18*, 103018.
[15] M. T. Mądzik, A. Laucht, F. E. Hudson, A. M. Jakob, B. C. Johnson, D. N. Jamieson, K. M. Itoh, A. S. Dzurak, A. Morello, *Nat. Commun.* **2021**, *12*, 181.

 © 2021 The Authors. Advanced Materials published by Wiley-VCH GmbH

[16] M. T. Mądzik, S. Asaad, A. Youssry, B. Joecker, K. M. Rudinger, E. Nielsen, K. C. Young, T. J. Proctor, A. D. Baczewski, A. Laucht, V. Schmitt, F. E. Hudson, K. M. Itoh, A. M. Jakob, B. C. Johnson, D. N. Jamieson, A. S. Dzurak, C. Ferrie, R. Blume-Kohout, A. Morello, arXiv: 2106.03082, **2021**.
[17] D. N. Jamieson, C. Yang, T. Hopf, S. M. Hearne, C. I. Pakes, S. Prawer, M. Mitic, E. Gauja, S. E. Andresen, F. E. Hudson, A. S. Dzurak, R. G. Clark, *Appl. Phys. Lett.* **2005**, *86*, 202101.
[18] J. van Donkelaar, C. Yang, A. D. C. Alves, J. C. McCallum, C. Hougaard, B. C. Johnson, F. E. Hudson, A. S. Dzurak, A. Morello, D. Spemann, D. N. Jamieson, *J. Phys.: Condens. Matter* **2015**, *27*, 154204.
[19] L. Rubin, J. Poate, *Ind. Phys.* **2003**, *9*, 12.
[20] W. Yuguang, Z. Tonghe, L. Yan, *Nucl. Instrum. Methods Phys. Res. B: Beam Inter. Mater. Atoms* **1998**, *135*, 570.
[21] D. R. McCamey, M. Francis, J. C. McCallum, A. R. Hamilton, A. D. Greentree, R. G. Clark, *Semicond. Sci. Technol.* **2005**, *20*, 363.
[22] T. Shinada, S. Okamoto, T. Kobayashi, I. Ohdomari, *Nature* **2005**, *437*, 1128.
[23] H. Bracht, H. H. Silvestri, I. D. Sharp, E. E. Haller, *Phys. Rev. B* **2007**, *75*, 035211.
[24] T. Luehmann, R. John, R. Wunderlich, J. Meijer, S. Pezzagna, *Nat. Commun.* **2019**, *10*, 4956.
[25] J. A. Gross, *Phys. Rev. Lett.* **2021**, *127*, 010504.
[26] S. Asaad, V. Mourik, B. Joecker, M. A. Johnson, A. D. Baczewski, H. R. Firgau, M. T. Mądzik, V. Schmitt, J. J. Pla, F. E. Hudson, K. M. Itoh, J. C. McCallum, A. S. Dzurak, A. Laucht, A. Morello, *Nature* **2020**, *579*, 205.
[27] J. A. Gross, C. Godfrin, A. Blais, E. Dupont-Ferrier, arXiv: 2103.08548, **2021**.
[28] G. Wolfowicz, A. M. Tyryshkin, R. E. George, H. Riemann, N. V. Abrosimov, P. Becker, H.-J. Pohl, M. L. Thewalt, S. A. Lyon, J. J. Morton, *Nat. Nanotechnol.* **2013**, *8*, 561.
[29] F. A. Mohiyaddin, R. Rahman, R. Kalra, G. Klimeck, L. C. Hollenberg, J. J. Pla, A. S. Dzurak, A. Morello, *Nano Lett.* **2013**, *13*, 1903.
[30] K. Groot-Berning, T. Kornher, G. Jacob, F. Stopp, S. T. Dawkins, R. Kolesov, J. Wrachtrup, K. Singer, F. Schmidt-Kaler, *Phys. Rev. Lett.* **2019**, *123*, 106802.
[31] P. Räcke, R. Staacke, J. W. Gerlach, J. Meijer, D. Spemann, *J. Phys. D: Appl. Phys.* **2019**, *52*, 305103.
[32] Y. Wang, Y. Zhao, A. Qayyum, G. Xiao, *Nucl. Instrum. Methods Phys. Res. B: Beam Inter. Mater. Atoms* **2007**, *265*, 474.
[33] Z. Xu, L. Zeng, Y. Zhao, J. Wang, Y. Wang, X. Zhang, G. Xiao, F. Li, *Laser Part. Beams* **2012**, *30*, 319.
[34] T. Shinada, A. Ishikawa, M. Fujita, K. Yamashita, I. Ohdomari, *Jpn. J. Appl. Phys.* **1999**, *38*, 3419.
[35] N. Cassidy, P. Blenkinsopp, I. Brown, R. J. Curry, B. N. Murdin, R. Webb, D. Cox, *Phys. Status Solidi A* **2021**, *218*, 2000237.
[36] M. B. H. Breese, P. J. C. King, G. W. Grime, F. Watt, *J. Appl. Phys.* **1992**, *72*, 2097.
[37] D. N. Jamieson, W. I. L. Lawrie, F. E. Hudson, A. S. Dzurak, A. Morello, S. G. Robson, A. M. Jakob, B. C. Johnson, J. C. McCallum, in *2016 21st Int. Conf. on Ion Implantation Technology (IIT)*, American Institute of Physics, Melville, NY, USA **2016**, pp. 299–304.
[38] J. L. Pacheco, M. Singh, D. L. Perry, J. R. Wendt, G. Ten Eyck, R. P. Manginell, T. Pluym, D. R. Luhman, M. P. Lilly, M. S. Carroll, E. Bielejec, *Rev. Sci. Instrum.* **2017**, *88*, 123301.
[39] D. N. Jamieson, W. I. Lawrie, S. G. Robson, A. M. Jakob, B. C. Johnson, J. C. McCallum, *Mater. Sci. Semicond. Process.* **2017**, *62*, 23.
[40] G. Tosi, F. A. Mohiyaddin, V. Schmitt, S. Tenberg, R. Rahman, G. Klimeck, A. Morello, *Nat. Commun.* **2017**, *8*, 450.
[41] G. Bertuccio, P. Rehak, D. Xi, *Nucl. Instrum. Methods Phys. Res., Sect. A* **1993**, *326*, 71.
[42] nanoanalytik GmbH, AFMinSEM, https://www.nanoanalytik.net/products/systems/afm-in-sem/ (accessed: February 2020).
[43] W. Majstrzyk, A. Ahmad, T. Ivanov, A. Reum, T. Angelow, M. Holz, T. Gotszalk, I. W. Rangelow, *Sens. Actuators A* **2018**, *276*, 237.
[44] G. Binnig, C. F. Quate, C. Gerber, *Phys. Rev. Lett.* **1986**, *56*, 930.
[45] R. E. J. Watkins, P. Rockett, S. Thoms, R. Clampitt, R. Syms, *Vacuum* **1986**, *36*, 961.
[46] L. Evensen, A. Hanneborg, B. S. Avset, M. Nese, *Nucl. Instrum. Methods Phys. Res., Sect. A* **1993**, *337*, 44.
[47] B. Johnson, J. McCallum, L. W. van Beveren, E. Gauja, *Thin Solid Films* **2010**, *518*, 2524.
[48] A. Morello, J. J. Pla, F. A. Zwanenburg, K. W. Chan, K. Y. Tan, H. Huebl, M. Möttönen, C. D. Nugroho, C. Yang, J. A. van Donkelaar, A. D. C. Alves, D. N. Jamieson, C. C. Escott, L. C. L. Hollenberg, R. G. Clark, A. S. Dzurak, *Nature* **2010**, *467*, 687.
[49] G. Betta, M. Boscardin, G. U. Pignatel, G. Verzellesi, L. Bosisio, L. Ferrario, M. Zen, G. Soncini, *Nucl. Instrum. Methods Phys. Res., Sect. A* **1998**, *409*, 346.
[50] G.-F. Betta, G. U. Pignatel, G. Verzellesi, M. Boscardin, A. Fazzi, L. Bosisio, *Nucl. Instrum. Methods Phys. Res., Sect. A* **2001**, *458*, 275.
[51] C. Fiorini, M. Porro, *IEEE Trans. Nucl. Sci.* **2005**, *52*, 1647.
[52] Hamamatsu Photonics K.K., Fast recovery Si PIN photodiode s9055-01, https://www.hamamatsu.com/jp/en/product/type/S9055-01/index.html (accessed: February 2020).
[53] J. P. Biersack, L. G. Haggmark, *Nuclear Instr. Methods* **1980**, *174*, 257.
[54] J. F. Ziegler, M. D. Ziegler, J. P. Biersack, *Nuclear Instr. Methods Phys. Res. B: Beam Interactions Mater. Atoms* **2010**, *268*, 1818.
[55] A. Rossi, T. Tanttu, F. E. Hudson, Y. Sun, M. Möttönen, A. S. Dzurak, *J. Vis. Exp.* **2015**, *100*, e52852.
[56] J. F. Ziegler, J. P. Biersack, *The Stopping and Range of Ions in Matter*, Springer, Boston, MA, USA **1985**, pp. 93–129.
[57] M. Posselt, M. Mäder, R. Grötzschel, M. Behar, *Appl. Phys. Lett.* **2003**, *83*, 545.
[58] M. Posselt, L. Bischoff, D. Grambole, F. Herrmann, *Appl. Phys. Lett.* **2006**, *89*, 151918.
[59] W. Pilz, J. Borany, R. Grötzschel, W. Jiang, M. Posselt, B. Schmidt, *Nucl. Instrum. Methods Phys. Res., Sect. A* **1998**, *419*, 137.
[60] O. S. Oen, M. T. Robinson, *Nuclear Instr. Methods* **1976**, *132*, 647.
[61] H. O. Funsten, S. M. Ritzau, R. W. Harper, R. Korde, *IEEE Trans. Nucl. Sci.* **2001**, *48*, 1785.
[62] H. O. Funsten, S. M. Ritzau, R. W. Harper, J. E. Borovsky, R. E. Johnson, *Phys. Rev. Lett.* **2004**, *92*, 213201.
[63] M. Robinson, in *Proceedings of the British Nuclear Energy Society*, British Nuclear Energy Society, London, UK **1970**.
[64] S. Ruffell, I. V. Mitchell, P. J. Simpson, *J. Appl. Phys.* **2005**, *97*, 123518.

© 2021 The Authors. Advanced Materials published by Wiley-VCH GmbH